

available at www.sciencedirect.comjournal homepage: www.elsevier.com/locate/ijrefrig

A new analytical and dynamical model of a scroll compressor with experimental validation

B. Blunier^{a,*}, G. Cirrincione^b, Y. Hervé^c, A. Miraoui^a

^aUniversity of Technology of Belfort-Montbéliard, Systems and Transport Laboratory, Rue Thierry Mieg, 90000 Belfort, France

^bDipartimento di Ingegneria Elettrica Industriale Politecnico di Torino, 10129 Torino, Italy

^cInESS, ULP/CNRS - UMR 7163, 23 rue de Loess, 67200 Strasbourg, France

ARTICLE INFO

Article history:

Received 18 August 2007

Received in revised form

25 November 2008

Accepted 28 November 2008

Published online 7 December 2008

Keywords:

Scroll compressor

Geometry

Thermodynamic

Modelling

Simulation

Calculation

Leakage

Comparison

Experiment

ABSTRACT

This paper deals with the scroll compressor, which is a machine used for compressing air or refrigerant. By using a novel reference frame, it proposes an original way of describing the geometry of the scroll wraps (represented as circle involutes) in which the symmetries are exploited in order to establish a thermodynamic model of the scroll compressor. This approach allows the chamber volumes to be analytically described without any special assumption and takes into account the discharge as a non-symmetrical process.

The proposed geometric model is aimed to be coupled with the thermodynamic model by using the standardized VHDL-AMS language and should be then considered as preliminary to the scroll overall simulation and design of a functional virtual prototype.

Simulations and experiments have shown good agreement.

© 2008 Elsevier Ltd and IIR. All rights reserved.

Nouveau modèle analytique et dynamique d'un compresseur à spirale et validation expérimentale

Mots clés : Compresseur à spirale ; Modélisation ; Simulation ; Géométrie ; Thermodynamique ; Calcul ; Fuite ; Comparaison ; Expérimentation

1. Introduction

The scroll compressor is a device used for compressing air or refrigerant, which was originally invented in 1905 by a French

engineer named Léon Creux (Creux, 1905). The device consists of two nested identical scrolls constituted in the classical design by involutes of circle as shown in Fig. 1. The two scrolls, whose axes of rotation do not meet each other, are assembled

* Corresponding author. Tel.: +33(0)3 84 58 33 98.

E-mail address: benjamin.blunier@utbm.fr (B. Blunier).

0140-7007/\$ – see front matter © 2008 Elsevier Ltd and IIR. All rights reserved.

doi:10.1016/j.ijrefrig.2008.11.009

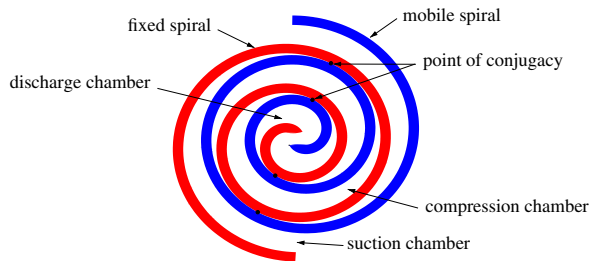


Fig. 1 – Schematic view of a scroll compressor.

with a relative angle of π , so that they can touch themselves at different points and form a series of growing size chambers.

The main advantages of the scroll compressor are the small number of moving parts, a high efficiency and a low level of noise and vibrations. Moreover, due to their low rotational speed, off-the-shelf electrical machines, like induction machines or brushless internal mounted permanent magnets machines, can be used in variable speed drives with high performance control strategies (Blunier et al., 2008a,b). For these reasons, the authors have shown that the scroll compressor can be a very good solution for the air management of fuel cell systems (Blunier and Miraoui, in press). However, one of the main problems when developing scroll compressors is the design of the scroll profile, which plays a key role in their performance.

Most of the models of the scroll compressor are based on a geometrical description which develops a relationship between the volumes and the leakage areas as a function of the orbiting angle. The computation of the geometry allows pressure, temperature and mass flows to be computed in each chamber of the compressor.

Many geometric shapes for scroll compressors have been investigated in a lot of papers and patents. Most works have mainly focused on the interpolating curves by using circle involutes (Lee and Wu, 1995; Hirano et al., 1990; Chen et al., 2002; Halm, 1997). One of the authors (Gravensen et al., 1998; Gravensen and Henriksen, 2001) redefines the entire geometry of the spiral by means of two planar curves being the involute a special case.

The extended part of the scroll is studied in a great deal of papers (Lee and Wu, 1995; Liu et al., 1992) in order to have a perfect meshing profile (i.e., zero clearance volume) and to optimize the discharge process. Liu et al. (1992) propose a graphical method and Lee and Wu (1995) give an analytical method. The extended part of the scroll makes the description and the volume estimation of the discharge process very complex.

Morishita et al. (1984) are the first authors who propose an analytical description of the compression and discharge chamber volumes. Nieter studies the suction (Nieter, 1988) and discharge (Nieter and Gagne, 1992) processes more accurately. The discharge process is considered as a non-symmetrical process and takes into account the position of the discharge port.

Yanagisawa et al. (1990) yields general expressions of all chamber volumes of the scroll and builds a complete analytical model of the compressor in good agreement with experimental data.

Chen et al. (2002) builds a complete model in which the geometry description is mainly based on the Yanagisawa model. This model includes the two kinds of leakage (flank and radial) and also the thermodynamic analysis.

Yanagisawa and Chen consider a special case for the initial angle involutes, as mentioned by Wang in Wang et al. (2005) who has analysed this problem in a general frame. Unlike Nieter, these authors make the assumption of symmetric process, whereby the discharge port is always located at the central part of the two scrolls. This makes the discharge process similar (i.e., with the same pressures and temperatures) for the two last compression chambers.

This paper proposes an original way to describe the geometry of the scroll wraps (here represented as involutes of circle) in which the symmetries are easily exploited to establish a thermodynamic model of the scroll compressor. The advantages of the model are the following: (1) the chamber volumes are analytically described without assuming any special case for the initial involute angles, (2) the flank and radial leakages are taken into account, (3) the discharge process is not considered as symmetrical. However, the extended part of the scroll is assumed to be an arc of circle as proposed by most of the authors (Halm, 1997; Yanagisawa et al., 1990; Wang et al., 2005; Blunier et al., 2006).

The next section deals with the geometrical description of the scroll, together with its validation. A novel reference frame is here introduced and the points of conjugacy are expressed. Section 3 describes the compression process in detail. Section 4 and 5 deal with the estimation of the chamber volumes and the leakages between them, respectively. The discharge process is also analysed in detail. Section 6 describes the thermodynamic model of the chambers and leakages components. Section 7 presents shortly the multi-discipline simulation language VHDL-AMS and the simulation process followed by a comparison between simulation and experimental results; the model shows good agreements with experiments.

The last section concludes the scroll compressor model with prospects for improving the model.

2. Geometrical description of the scroll

The shape of the investigated scroll can be described by an involute of circle. The fixed and orbiting scrolls are therefore both defined as two involutes that develop around a basic circle with radius r_b and are offset by a constant distance. Many authors describe the geometry using the intrinsic equation (i.e., an equation that links the arc-length and the tangent direction) (Bush and Beagle, 1992; Halm, 1997) or parametric equations (Lee and Wu, 1995; Wang et al., 2005). A new way to describe the geometry, based on the ideas of Gravensen (Gravensen and Henriksen, 2001), is proposed here. This framework makes all the properties of the scroll appear very clearly. Each involute (see Fig. 2) is defined by introducing the orthonormal frame (t, n) :

$$t(\varphi) = (\cos \varphi, \sin \varphi), \quad (1a)$$

$$n(\varphi) = (-\sin \varphi, \cos \varphi). \quad (1b)$$

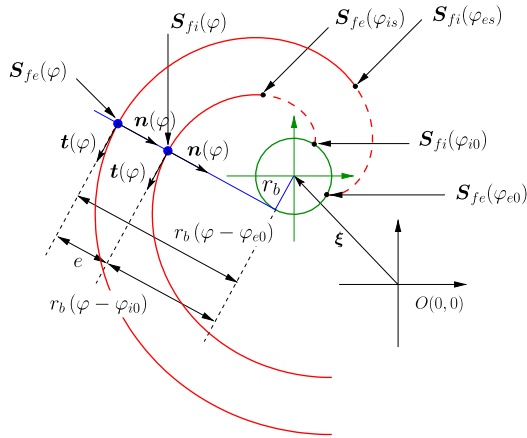


Fig. 2 – Scroll geometry.

where $\mathbf{t}(\varphi)$ is the unit tangent vector and $\mathbf{n}(\varphi)$ the unit normal vector, as seen in Fig. 2.

The involute of a circle is given by:

$$\mathbf{S}_{xy}(\varphi) = \underbrace{r_b \mathbf{t}(\varphi)}_{\text{center of the radius of curvature}} - \underbrace{r_b(\varphi - \varphi_{y0}) \mathbf{n}(\varphi)}_{\text{radius of curvature}} + \underbrace{\xi}_{\text{eccentricity}} \quad (2)$$

where r_b is the involute basic circle radius, φ is the involute angle, φ_{y0} the internal or external involute initial angle with $x \in \{f, m\}$ and $y \in \{i, e\}$.

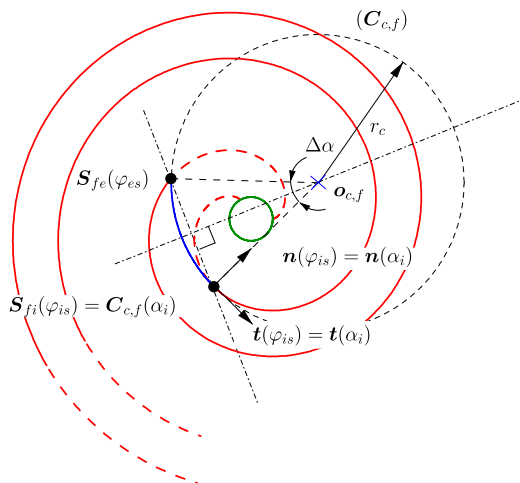
The arc-length l of the involute of a circle is given by its intrinsic equation (Gravensen and Henriksen, 2001):

$$\frac{dl}{d\varphi} = \rho(\varphi) = r_b(\varphi - \varphi_{y0}). \quad (3)$$

where $\rho(\varphi)$ is the radius of curvature of the involute.

2.1. Fixed scroll

From (2), the representation of the fixed (f) scroll can be determined as follows:

Fig. 3 – Interpolating circle construction $C_{c,f}$.

$$\mathbf{S}_{fe}(\varphi) = r_b \mathbf{t}(\varphi) - r_b(\varphi - \varphi_{e0}) \mathbf{n}(\varphi) \quad \forall \varphi \in I_e = [\varphi_{es}, \varphi_{max}], \quad (4)$$

$$\mathbf{S}_{fi}(\varphi) = r_b \mathbf{t}(\varphi) - r_b(\varphi - \varphi_{i0}) \mathbf{n}(\varphi) \quad \forall \varphi \in I_i = [\varphi_{is}, \varphi_{max}]. \quad (5)$$

where \mathbf{S}_{fe} and \mathbf{S}_{fi} are, respectively, the external (e) and internal (i) involutes. The angles φ_{es} and φ_{is} are the external and internal starting angles, φ_{max} the involute ending angle, φ_{e0} and φ_{i0} the initial angles of the external and internal involutes as seen in Fig. 2. The domains of definition of the internal and external involutes are, respectively, I_i and I_e .

The thickness of the scroll is given by for $\varphi \in I_e \cap I_i$:

$$e = \|\mathbf{S}_{fi} - \mathbf{S}_{fe}\| = r_b(\varphi_{i0} - \varphi_{e0}). \quad (6)$$

By definition, $r_b > 0$ and $\varphi_{i0} > \varphi_{e0}$.

2.2. Interpolating circle

In order to complete the scroll shape representation, $\mathbf{S}_{fi}(\varphi_{is})$ and $\mathbf{S}_{fe}(\varphi_{es})$ have to be connected (see Fig. 2). Many authors (Chen et al., 2002; Morishita et al., 1984; Yanagisawa et al., 1990; Wang et al., 2005) propose a simple approach without describing it: the two points are connected by an arc of a circle $C_{c,f}$ of radius r_c .

Other authors (Lee and Wu, 1995, 1996; Zhenquan et al., 1994) study the extended part of the scroll in order to have no clearance volume at the end of the compression process; this is called the perfect meshing profile (PMP).

For the investigated compressor the extended part can be described by an arc of a circle (see Fig. 4). The circle is represented by:

$$\mathbf{C}_{c,f}(\alpha) = \mathbf{o}_{c,f} - r_c \mathbf{n}(\alpha), \quad (7)$$

where $\mathbf{o}_{c,f}$ and r_c are, respectively, the centre and the radius of the circle.

The circle parameters are computed under the two following constraints:

- (1) $C_{c,f}$ passing through $\mathbf{S}_{fi}(\varphi_{is})$ and $\mathbf{S}_{fe}(\varphi_{es})$.
- (2) No discontinuity of the derivative at $\mathbf{S}_{fi}(\varphi_{is})$ between the spiral \mathbf{S}_{fi} and the circle $C_{c,f}$.

The second constraint implies (see Fig. 3):

$$\mathbf{t}(\alpha_i) = \mathbf{t}(\varphi_{is}) \Rightarrow \alpha_i \equiv \varphi_{is} \pmod{2\pi} \quad (8)$$

The two constraints yield the following expression for the circle radius:

$$r_c = \frac{r_b(2 + \xi_1^2 + \xi_2^2 - 2(1 + \xi_1 \xi_2) \cos \xi_3 - 2(\xi_2 - \xi_1) \sin \xi_3)}{2(\xi_2 - \xi_1 \cos \xi_3 - \sin \xi_3)}, \quad (9)$$

where $\xi_1 = \varphi_{es} - \varphi_{e0}$, $\xi_2 = \varphi_{is} - \varphi_{i0}$ and $\xi_3 = \varphi_{is} - \varphi_{es}$.

Hence, $\mathbf{o}_{c,f}$ is deduced:

$$\mathbf{o}_{c,f} = r_b \mathbf{t}(\varphi_{is}) + (r_c - r_b(\varphi_{is} - \varphi_{i0})) \mathbf{n}(\varphi_{is}). \quad (10)$$

The domain of definition I_c of the interpolating circle is the following (see Fig. 3):

$$I_c = [\varphi_{is} - \Delta\alpha, \varphi_{is}] \quad (11a)$$

where

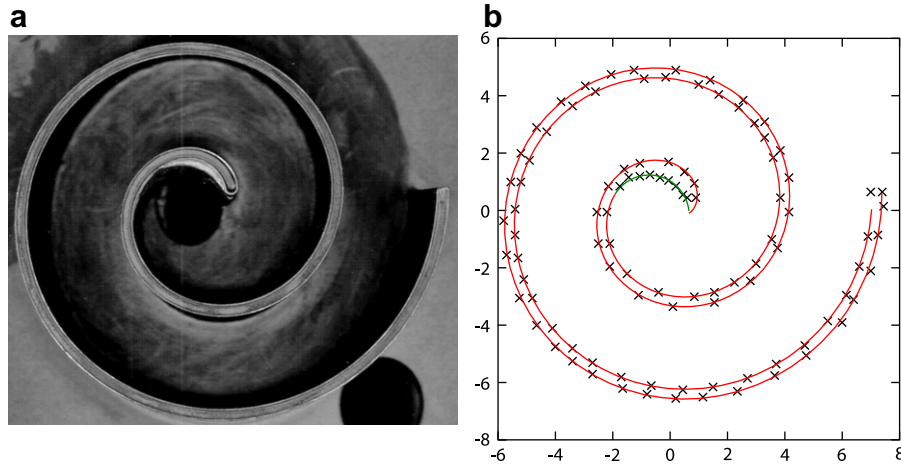


Fig. 4 – Experimental validation of the geometry model.

$$\Delta\alpha = a \cos\left(\frac{1}{r_c^2}(\mathbf{S}_{fi}(\varphi_{is}) - \mathbf{o}_{cf}) \cdot (\mathbf{S}_{fe}(\varphi_{es}) - \mathbf{o}_{cf})\right) \quad (11b)$$

$$= a \cos\left(1 - \frac{r_b}{r_c}(\xi_2 - \xi_1 \cos \xi_3 + \sin \xi_3)\right) \quad (11c)$$

where the symbol \cdot stands for the inner product.

2.3. Identification of the investigated scroll compressor

The geometry of the scroll has been validated on an air compressor used at the UTBM¹. The parameters in the nonlinear expressions (Blunier and Miraoui, in press; Lee and Wu, 1995; Chen et al., 2002) can be identified by minimizing a nonlinear least squares error function by means of the second-order trust-region method called Levenberg-Marquardt (Haykin, 1998). Fig. 4 shows the obtained results.

2.4. Orbiting scroll

The geometry of the orbiting scroll is the same as the fixed one but is offset by π (see Fig. 1 page 1) and the two scrolls are in conjugacy.

Defining θ as the orbiting angle, it follows:

$$\mathbf{S}_{me}(\varphi) = -\mathbf{S}_{fe}(\varphi) - r_o \mathbf{n}(\theta) \quad \forall \varphi \in \mathbf{I}_e = [\varphi_{es}, \varphi_{max}] \quad (12)$$

$$\mathbf{S}_{mi}(\varphi) = -\mathbf{S}_{fi}(\varphi) - r_o \mathbf{n}(\theta) \quad \forall \varphi \in \mathbf{I}_i = [\varphi_{is}, \varphi_{max}] \quad (13)$$

where $r_o = r_b(\varphi_{e0} - \varphi_{i0} + \pi)$ is the orbiting radius.

2.5. Novel reference frame

In literature the reference frame shown in Fig. 5(a) is employed. Here a novel reference frame is presented (see Fig. 5(b)) in order to exploit the symmetry of the two scrolls. In this frame, the representation of the fixed scroll is given by:

$$\tilde{\mathbf{S}}_{fi}(\varphi, \theta) = r_b \mathbf{t}(\varphi) - r_b(\varphi - \varphi_{i0}) \mathbf{n}(\varphi) + \frac{1}{2} r_o \mathbf{n}(\theta) \quad (14)$$

$$\tilde{\mathbf{S}}_{fe}(\varphi, \theta) = r_b \mathbf{t}(\varphi) - r_b(\varphi - \varphi_{e0}) \mathbf{n}(\varphi) + \frac{1}{2} r_o \mathbf{n}(\theta). \quad (15)$$

The orbiting scroll is given by:

$$\tilde{\mathbf{S}}_{mi}(\varphi, \theta) = -\tilde{\mathbf{S}}_{fi}(\varphi, \theta) \quad (16)$$

$$\tilde{\mathbf{S}}_{me}(\varphi, \theta) = -\tilde{\mathbf{S}}_{fe}(\varphi, \theta) \quad (17)$$

2.6. Points of conjugacy

The k th point of conjugacy $\varphi_{ci,k}$ at the internal involute is determined by:

$$\varphi_{ci,k} = \theta + 2(k-1)\pi \quad \forall k \in \{1 \dots 3\}. \quad (18)$$

The k th point of conjugacy $\varphi_{ce,k}$ at the external involute is determined by:

$$\varphi_{ce,k} = \theta - \pi + 2(k-1)\pi \quad \forall k \in \{1 \dots 3\} \quad (19)$$

The point of conjugacy exists if and only if both $\varphi_{ci,k}$ and $\varphi_{ce,k}$ exist, that is:

$$\exists \varphi_{ci,k} \Leftrightarrow \exists \varphi_{ce,k} \quad (20a)$$

Then

$$\exists \varphi_{ci,k} \wedge \exists \varphi_{ce,k} \Leftrightarrow (\varphi_{ci,k} \in \mathbf{I}_i) \wedge (\varphi_{ce,k} \in \mathbf{I}_e) \quad (20b)$$

Finally, (20a) holds if and only if

$$\max(\varphi_{is} - 2(k-1)\pi, \varphi_{es} + \pi - 2(k-1)\pi) \leq \theta \leq \varphi_{max} - 2(k-1)\pi. \quad (20c)$$

Hence, for the investigated compressor, with $k \in \{1 \dots 3\}$:

$$\exists \varphi_{cx,1} \Leftrightarrow \theta \geq \theta^{\text{dis}} \quad \theta^{\text{dis}} = \max(\varphi_{is}, \varphi_{es} + \pi) \quad (21a)$$

$$\exists \varphi_{cx,2} \Leftrightarrow \forall \theta \quad (21b)$$

¹ Université de Technologie de Belfort-Montbéliard, France.

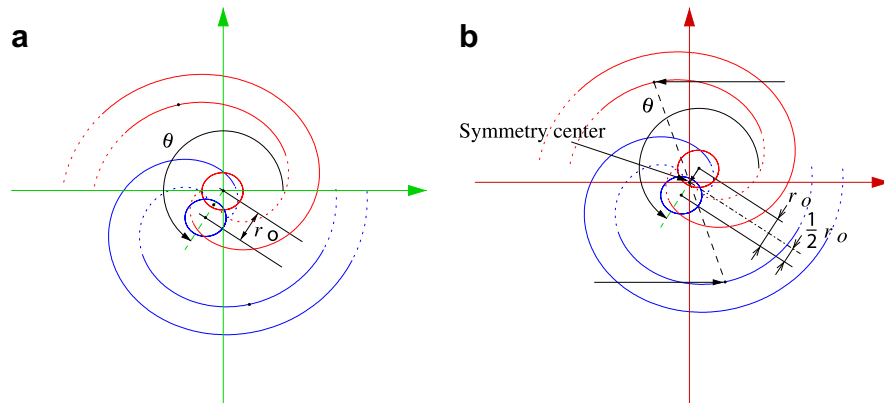


Fig. 5 – Scroll reference frames.

$$\exists \varphi_{cx,3} \Leftrightarrow \theta \leq \theta^{\text{suc}} \quad \theta^{\text{suc}} = \varphi_{\text{max}} - 4\pi \quad (21c)$$

where θ^{dis} and θ^{suc} are, respectively, the discharge (i.e., when the compression chamber opens in the discharge chamber) and suction angles (i.e., when the suction chamber closes and becomes the compression chamber).

3. Compression process description

The compression process can be described by the four positions of the orbiting scroll shown in Fig. 6.

During the process θ varies from 2π to 0. At each time instant during the compression six chambers can be defined:

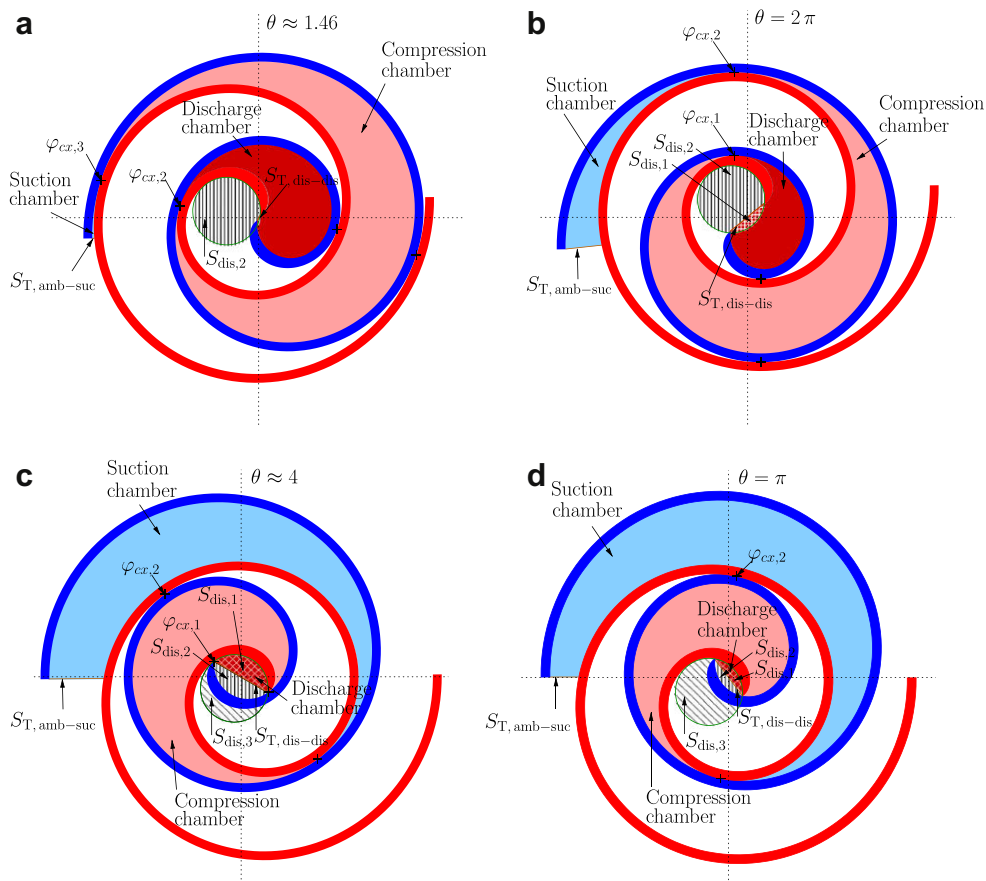


Fig. 6 – Compression process description.

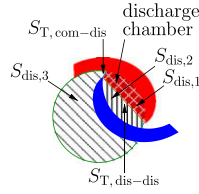


Fig. 7 – Zoom on the discharge area.

- (1) two suction chambers,
- (2) two compression chambers,
- (3) two discharge chambers.

Thanks to the geometry of the compressor, the pairs of suction, compression and discharge chambers have the same volume. All the chambers are separated either by contact points or by leakage flow areas if the contact point does not exist.

As seen in Fig. 6, even if the volumes of each pair of pockets are the same, the compression process cannot be considered as symmetrical because of the position of the discharge port. For example, in Fig. 6(c), one of the compression chambers is connected to the discharge port and the leakage area between the discharge port and the compression chamber is given by $S_{dis,3}$. The other compression chamber is not connected to the discharge port and consequently the pressures of the two compression chambers differ.

Some authors (Halm, 1997; Chen et al., 2002) consider the case in which the compression chamber starts to open in the discharge chamber by treating each region of different pressure as an individual control volume as long as the pressures do not equalise. When the pressure between the two former compression chambers and the discharge

chamber (considered as one chamber in these references) equalise, the region composed of the three chambers is treated as one control volume. This description makes the process complex because the topology (i.e., the number of control volumes) is changing during the compression. Here, it is always assumed the same number of control volumes even if the pressures of the chambers are the same. This makes the description simpler for the simulation of the compressor (fixed topology).

The compression process is considered as periodic. One period can be described by the following steps:

- (1) At the start of the suction, the volume of the suction chamber is zero and the volume of the compression chamber is maximum. Suction starts for $\theta = \theta^{suc}$ when the contact point $\varphi_{cx,3}$ appears. The position a short time after the suction process starts is given by Fig. 6(a). Leakages occur through the following leakage flow areas:
 - $S_{T,dis-dis}$ between the two discharge chambers,
 - $S_{dis,1}$ and $S_{dis,2}$ between the discharge chambers and the discharge port.
- (2) The compression chamber is enclosed between two contact points depending on the orbiting angle θ : $\varphi_{cx,3}$ and $\varphi_{cx,2}$ (Fig. 6(a)) or $\varphi_{cx,2}$ and $\varphi_{cx,1}$ (Fig. 6(b)). Leakages occur through the following leakage flow areas:
 - $S_{T,amb-suc}$ between the outside of the compressor and the suction chamber,
 - $S_{T,dis-dis}$ between the two discharge chambers,
 - $S_{dis,1}$ and $S_{dis,2}$ between the discharge chambers and the discharge port.
- (3) One of the compression chambers is connected to the discharge port and leakages occur through $S_{dis,3}$ (Fig. 6(c)). The discharge process becomes asymmetric.

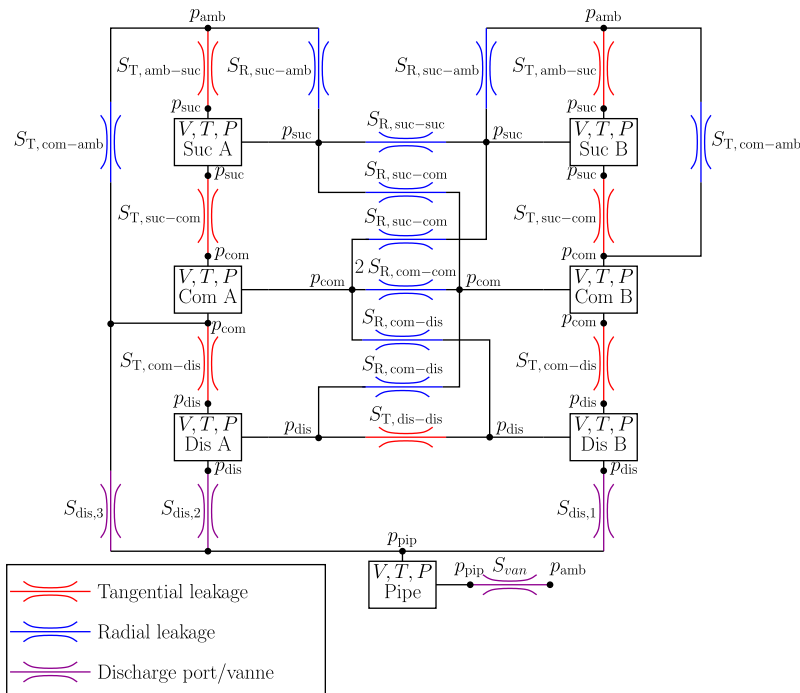


Fig. 8 – Compressor model.

- (4) The compression chambers open to the discharge chambers when the contact point $\varphi_{cx,1}$ disappears at $\theta = \theta^{\text{dis}}$, (start of discharge). Tangential leakages through the flow area $S_{T,\text{com-dis}}$ occur between the compression chambers and discharge chambers (Fig. 6(d) and Fig. 7).
- (5) The process restarts at $\theta = \theta^{\text{suc}}$. At this angle the former suction chamber becomes the compression chamber and the compression chamber becomes the discharge chamber. The end conditions (pressure and temperature) of the suction and compression chambers become, respectively, the initial conditions of the compression and discharge chambers.

Finally, a component-based representation of the scroll compressor (see Fig. 8) can be built in order to compute the dynamic behaviour of the compressor by means of a simulation software. As explained previously, the topology of the representation is fixed: the number of components and the interconnections do not change during the process. The compressor is represented with the help of two kinds of components: the control volumes represented by boxes and the leakages represented as isentropic flows.

To complete the model of the compressor the geometric law of the components have to be computed. These laws are the following:

- For a control volume component: $V = f(\theta)$ where V is its volume.
- For a leakage flow area component: $S = g(\theta)$ where S is its flow area.

4. Geometrical description of the chamber volumes

4.1. General expression of the area enclosed by an involute of a circle

Fig. 9. The analytical expression of the area enclosed between φ_1 and φ_2 of an involute of a circle is obtained by solving the following integral:

$$\int_{\varphi_1}^{\varphi_2} \|S_{xy} \times S'_{xy}\| d\varphi = f(\varphi_{y0}, \varphi_1, \varphi_2, \theta) \quad (22)$$

where $x \in m, f$ and $y \in i, e$.

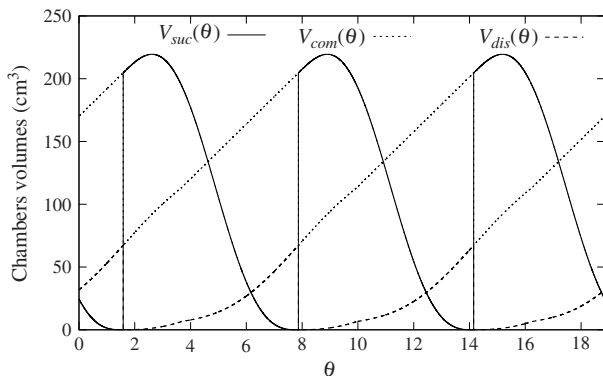


Fig. 9 – Chambers volumes vs. orbiting angle.

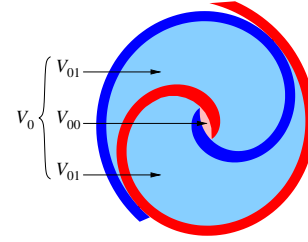


Fig. 10 – Volumes of the central chamber.

$$f(\varphi_{y0}, \varphi_1, \varphi_2, \theta) = \frac{r_b^2}{3} \left((\varphi_2 - \varphi_{y0})^3 - (\varphi_1 - \varphi_{y0})^3 \right) - \frac{r_b r_o}{2} \left[\cos(\theta - \varphi_2) - \cos(\theta - \varphi_1) - (\varphi_2 - \varphi_{y0}) \sin(\theta - \varphi_2) + (\varphi_1 - \varphi_{y0}) \sin(\theta - \varphi_1) \right] \quad (23)$$

4.2. Central chamber

The central chamber volume V_0 can be divided into three volumes as seen in Fig. 10.

$$V_0(\theta) = h \left(\int_{\varphi_{is}}^{\varphi_{ci,k}} \|\tilde{S}_{fi} \times \tilde{S}'_{fi}\| d\varphi - \int_{\varphi_{es}}^{\varphi_{ce,k}} \|\tilde{S}_{me} \times \tilde{S}'_{me}\| d\varphi \right) + V_{cl} \quad (24a)$$

$$\text{where } k = \begin{cases} 1 & \text{if } \exists \varphi_{ci,1} \\ 2 & \text{elsewhere} \end{cases}$$

$$= \begin{cases} h(f(\varphi_{i0}, \varphi_{is}, \theta, \theta) - f(\varphi_{e0}, \varphi_{es}, \theta - \pi, \theta)) + V_{cl} & \text{if } \theta \geq \theta^{\text{dis}} \\ h(f(\varphi_{i0}, \varphi_{is}, \theta + 2\pi, \theta) - f(\varphi_{e0}, \varphi_{es}, \theta + \pi, \theta)) + V_{cl} & \text{elsewhere} \end{cases}$$

$$V_{cl} = hr_c^2 \left(\pi - a \sin\left(\frac{2r_b}{r_c}\right) - \frac{2r_b}{r_c} \right) \quad (24b)$$

where V_{cl} is the clearance volume of the compressor given in Yanagisawa et al. (1990).

$$V_{00}(\theta) = hr_c[r_c \beta(\theta) - (r_c - l_{\text{dis}}(\theta)) \sin \beta] \quad (25a)$$

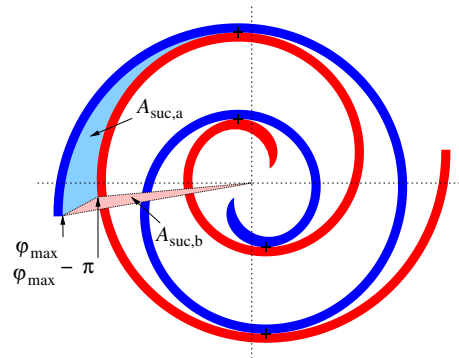


Fig. 11 – Suction volume computation.

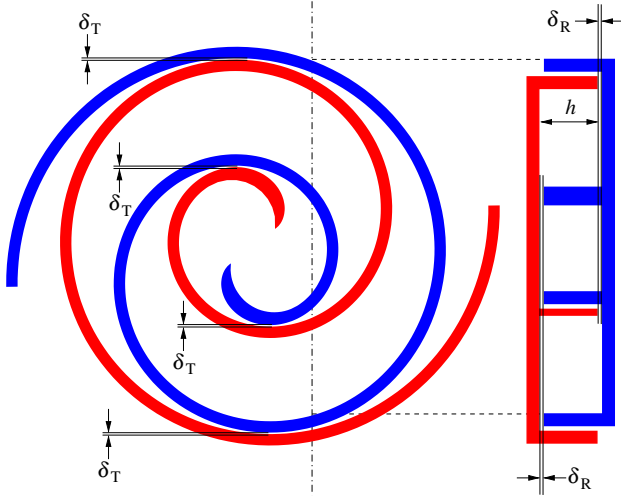


Fig. 12 – Two kinds of leakage: tangential (subscript T) and radial (subscript R).

$$\beta = \pi - a \cos\left(\frac{r_c - r_o + r_o \cos(\theta - \theta^{\text{dis}})}{r_c - l_{\text{dis}}}\right) - a \sin\left(\frac{2r_b}{r_c}\right) \quad (25b)$$

$$l_{\text{dis}} = \delta_T + r_c - \sqrt{r_o^2 + (r_c - r_o)^2 + 2r_o(r_c - r_o)\cos(\theta - \theta^{\text{dis}})} \quad (25c)$$

$$V_{01}(\theta) = \frac{1}{2}(V_0(\theta) - V_{00}(\theta)) \quad (26)$$

4.3. Suction chamber

The suction chamber volume computation is computed by adding the two volumes shown in Fig. 11. It has to be noticed that the area $A_{\text{suc},b}$ can be positive or negative, depending on the orbiting angle.

$$V_{\text{suc}}(\theta) = hA_{\text{suc}}(\theta) = h(A_{\text{suc},a}(\theta) + A_{\text{suc},b}(\theta)) \quad (27a)$$

where (see Fig. 11)

$$A_{\text{suc},a}(\theta) = \frac{1}{2} \int_{\varphi_{ci,k}}^{\varphi_{\text{max}}} \|\tilde{\mathbf{S}}_{fi} \times \tilde{\mathbf{S}}'_{fi}\| d\varphi - \frac{1}{2} \int_{\varphi_{ce,k}}^{\varphi_{\text{max}}-\pi} \|\tilde{\mathbf{S}}_{me} \times \tilde{\mathbf{S}}'_{me}\| d\varphi \quad (27b)$$

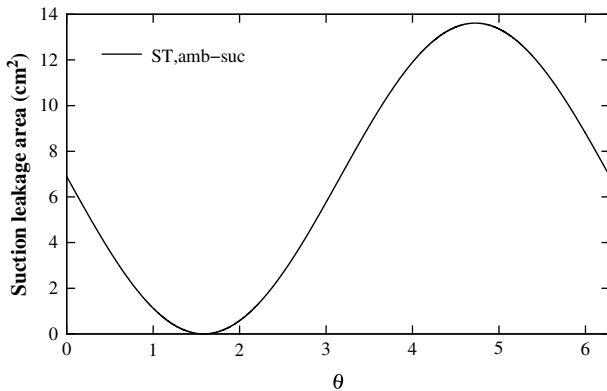


Fig. 13 – Suction leakage areas.

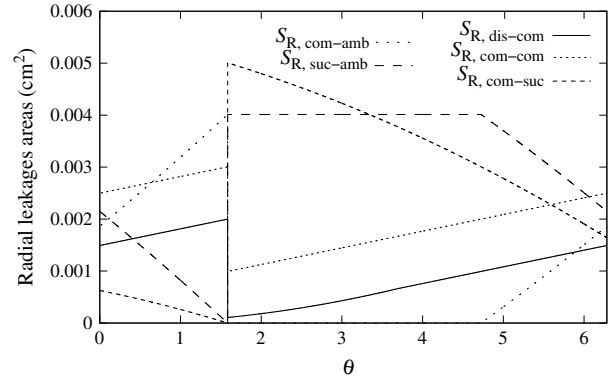


Fig. 14 – Radial leakages during the compression process.

$$\text{with } k = \begin{cases} 3 & \text{if } \exists \varphi_{ci,3} \\ 2 & \text{elsewhere} \end{cases}$$

$$= \begin{cases} \frac{1}{2}(f(\varphi_{i0}, \theta + 4\pi, \varphi_{\text{max}}, \theta) - f(\varphi_{e0}, \theta + 3\pi, \varphi_{\text{max}} - \pi, \theta)) & \text{if } \theta \leq \theta^{\text{suc}} \\ \frac{1}{2}(f(\varphi_{i0}, \theta + 2\pi, \varphi_{\text{max}}, \theta) - f(\varphi_{e0}, \theta + \pi, \varphi_{\text{max}} - \pi, \theta)) & \text{elsewhere} \end{cases}$$

$$A_{\text{suc},b}(\theta) = \frac{1}{2} \det(\tilde{\mathbf{S}}_{fi}(\varphi_{\text{max}}, \theta) \tilde{\mathbf{S}}_{me}(\varphi_{\text{max}} - \pi, \theta)) \quad (27c)$$

$$= \frac{r_b r_o}{4} (2 - 2\cos(\theta - \varphi_{\text{max}}) - (\varphi_{i0} + \varphi_{e0} + \pi - 2\varphi_{\text{max}})\sin(\theta - \varphi_{\text{max}}))$$

4.4. Compression chamber

The volume of the compression chamber is defined as the area enclosed by the involutes of the orbiting and the fixed scrolls between two conjugate points, multiplied by the height of the scroll. The compression chamber definition vs. the orbiting angle has been described in Section 3.

$$V_{\text{com}}(\theta) = \begin{cases} \frac{h}{2} \left(\int_{\varphi_{ci,k}}^{\varphi_{ci,k+1}} \|\tilde{\mathbf{S}}_{fi} \times \tilde{\mathbf{S}}'_{fi}\| d\varphi - \int_{\varphi_{ce,k}}^{\varphi_{ce,k+1}} \|\tilde{\mathbf{S}}_{me} \times \tilde{\mathbf{S}}'_{me}\| d\varphi \right) \\ V_{01}(\theta) & \text{elsewhere} \end{cases} \quad (28a)$$

where $k = \begin{cases} 1 & \text{if } \exists \varphi_{ci,1} \\ 2 & \text{if } \exists \varphi_{ci,3} \end{cases}$

$$= \begin{cases} hr_b r_o \pi (2\theta - \varphi_{e0} - \varphi_{i0} + \pi) & \text{if } \theta \geq \theta^{\text{dis}} \\ hr_b r_o \pi (2\theta - \varphi_{e0} - \varphi_{i0} + 5\pi) & \text{if } \theta \leq \theta^{\text{suc}} \\ V_{01}(\theta) & \text{elsewhere} \end{cases} \quad (28b)$$

4.5. Discharge chamber

The discharge chamber definition vs. the orbiting angle has been described in Section 3. The volume computation gives:

$$V_{\text{dis}}(\theta) = \begin{cases} \frac{1}{2}V_0(\theta) & \text{if } \exists \varphi_{ci,1} \vee \exists \varphi_{ci,3} \\ \frac{1}{2}V_{00}(\theta) & \text{elsewhere} \end{cases} \quad (29)$$

$$= \begin{cases} \frac{1}{2}V_0(\theta) & \text{if } (\theta \geq \theta^{\text{dis}}) \vee (\theta \leq \theta^{\text{suc}}) \\ \frac{1}{2}V_{00}(\theta) & \text{elsewhere} \end{cases}$$

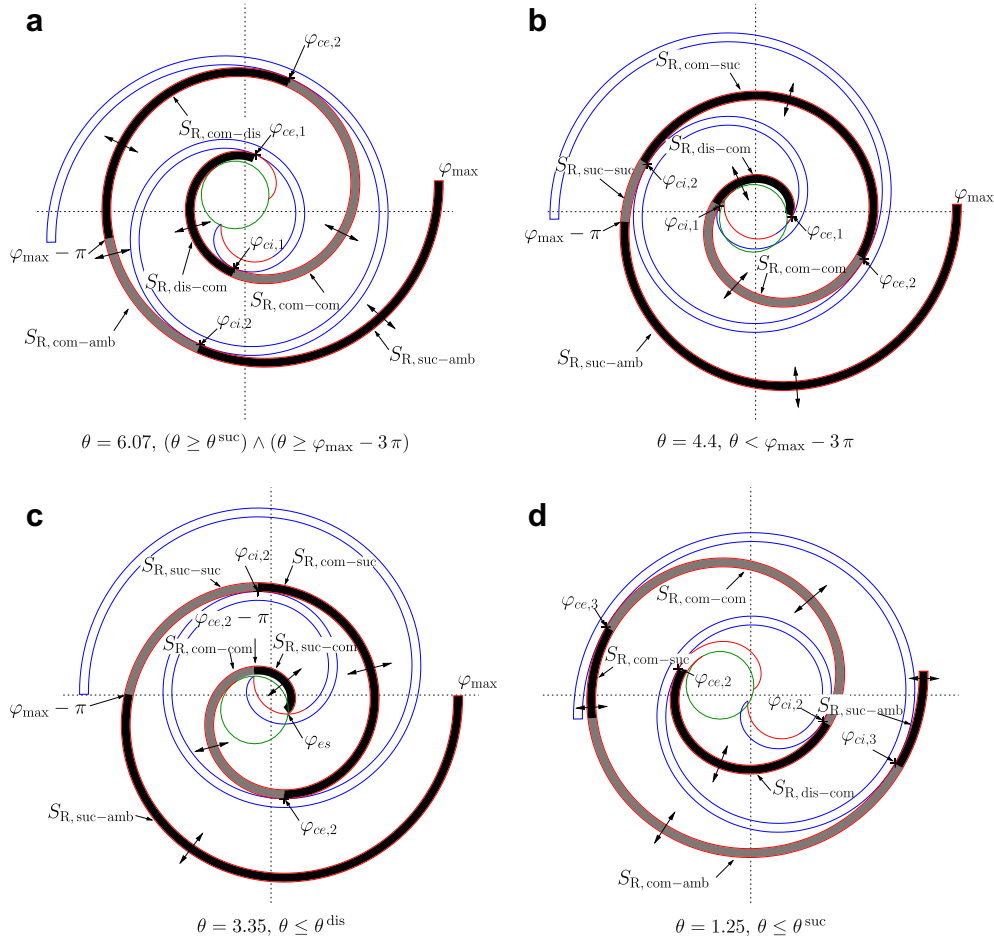


Fig. 15 – Radial leakages.

5. Leakage computation

For a real compressor, pressures in the chambers differ from ideal pressures because leakages occur between the chambers. On the one hand the leakages increase the energy consumption (i.e., compression work) because the gas which flows from a high pressure chamber to a low pressure chamber will be compressed again. On the other hand, the leakages decrease the volumetric efficiency.

Two kinds of leakage exist in the scroll compressor as illustrated in Fig. 12:

Tangential (of flank) leakages: the gas flows through the clearance (δ_T) between the flanks of the two scrolls (in the following, the tangential leakages between the chambers x and y are noted $S_{T,x-y}$);

Radial leakages: the gas flows through the clearance (δ_R) formed between each base plate and corresponding wrap tip (in the following, the radial leakages between the chambers x and y are noted $S_{R,x-y}$).

5.1. Tangential leakages

The suction and the discharge areas are treated as tangential leakages in the model.

When contact point exists between the chambers x and y , the leakage is computed as follows:

$$S_{T,x-y} = \delta_T h \quad (30)$$

where h represents the height of the spirals.

The suction leakage area (see Fig. 13) is given in Tojo et al. (1986):

$$S_{T,amb-suc}(\theta) = h(r_o(1 - \cos(\theta - \theta^{suc})) + \delta_T), \quad (31)$$

under the assumption that the curvature of the inner involute is neglected (i.e., it can be represented by a straight line).

The computation of the leakage area between the compression and discharge chambers (see Fig. 7) is given in Tojo et al. (1986). This leakage exists if and only if the compression chamber is opened in the discharge chamber (i.e., if no contact point exists between the chambers). Then, it follows:

$$S_{T,com-dis} = \begin{cases} \delta_T h & \text{if } \exists \varphi_{ci,1} \vee \exists \varphi_{ci,3} \\ h l_{dis}(\theta) & \text{elsewhere} \end{cases} \quad (32)$$

$$= \begin{cases} \delta_T h & \text{if } (\theta \geq \theta^{dis}) \vee (\theta \leq \theta^{suc}) \\ h l_{dis}(\theta) & \text{elsewhere} \end{cases}$$

where $l_{dis}(\theta)$ is given by (25c) page 15.

The leakage areas which are between the two discharge chambers are computed as follows:

$$S_{T,dis-dis} = 2 \left\| \tilde{S}_{fe}(\varphi_{es}) \right\|$$

$$= [4r_b^2(\varphi_{es}^2 - 2\varphi_{es}\varphi_{e0} + \varphi_{e0}^2 + 1) - 4r_b r_o((\varphi_{es} - \varphi_{e0})\cos(\theta - \varphi_{es}) + \sin(\theta - \varphi_{es})) + r_o^2]^{1/2} \quad (33)$$

5.2. Radial leakages

In most references (Halm, 1997; Wang et al., 2005), the authors assume which chamber has the biggest pressure. They calculate the area of the leakages assuming the direction of the leakage (in or out of the chamber). During the discharge process, the direction of the flow between the chambers is not known *a priori* especially when this process is not considered as symmetric. In the real discharge, the pressures in the two compression chambers are not equal.

As seen in Fig. 15 (page 1), the leakage section is different depending on the gas flows from the chamber x to y or vice versa. In one case, the leakage should be computed considering the arc-length of the internal spiral, and in the other case, considering the arc-length of the external spiral.

It is assumed here that the thickness of the scroll is small enough not to distinguish the two cases: the leakage area is the same if the gas flows from x to y or from y to x .

The mean arc-length l_{mean} of the spirals (sealing line length) is therefore used. The expression of the mean fixed spiral $\bar{S}_{\text{mean}}(\varphi)$ is given by:

$$\bar{S}_{\text{mean}}(\varphi) = r_b t(\varphi) - r_b \left(\varphi - \frac{\varphi_{i0} + \varphi_{e0}}{2} \right) n(\varphi) + \frac{1}{2} r_o n(\theta) \quad (34)$$

The arc-length is deduced from the intrinsic equation (3) of the spiral:

$$\frac{dl_{\text{mean}}(\varphi)}{d\varphi} = r_b \left(\varphi - \frac{\varphi_{i0} + \varphi_{e0}}{2} \right) = \rho(\varphi) \quad (35)$$

where ρ is the radius of curvature of the involute.

Then, the mean arc-length between the two angles φ_1 and φ_2 is computed as follows:

$$l_{\text{mean}}(\varphi_1 \rightarrow \varphi_2) = \int_{\varphi_1}^{\varphi_2} r_b \left(\varphi - \frac{\varphi_{i0} + \varphi_{e0}}{2} \right) d\varphi \quad (36a)$$

$$= \frac{1}{2} r_b (\varphi_2 - \varphi_1) (\varphi_1 + \varphi_2 - \varphi_{e0} - \varphi_{i0}) \quad (36b)$$

According to Figs. 8 and 15 (pages 1 and 1), six kinds of radial leakage exist.

To compute the leakages areas, several cases have to be distinguished:

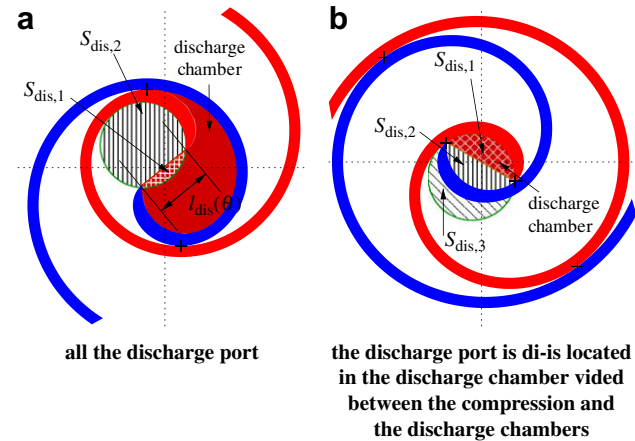


Fig. 16 – Discharge process description.

- (1) The first point of conjugacy $\varphi_{ci,1}$ exists (Fig. 15(a)).
- (2) The orbiting angle θ is smaller than $\varphi_{\text{max}} - 3\pi$ (Fig. 15(b)).
- (3) The two compression chambers open into the discharge chamber: $\varphi_{ci,1}$ does not exist anymore (Fig. 15(c)).
- (4) The last point of conjugacy $\varphi_{ci,3}$ exists (Fig. 15(d)).

For the second case, on the one hand, there is no leakage anymore between the compression chamber and the outside of the compressor: the leakages only occur between the compression chamber and the suction chamber; on the other hand leakage areas between the two suction chambers appear: the area is not computed because the pressures of both chambers are equal and no leakage occurs.

The different leakages are plotted as a function of the orbiting angle θ in Fig. 14.

5.2.1. Leakage between the discharge and the compression chambers

Radial leakages between the discharge and the compression chambers are computed in the case that $\varphi_{ce,1}$ exists (Fig. 15(a)) or $\varphi_{ce,3}$ exists (Fig. 15(d)). Then, it follows,

$$S_{R,\text{dis-com}} = \delta_R \int_{\varphi_1}^{\varphi_2} \rho(\varphi) d\varphi \text{ with } \begin{cases} \varphi_1 = \varphi_{ce,1} \text{ and } \varphi_2 = \varphi_{ci,1} & \text{if } \exists \varphi_{ce,1} \\ \varphi_1 = \varphi_{ce,2} \text{ and } \varphi_2 = \varphi_{ci,2} & \text{if } \exists \varphi_{ce,3} \\ \varphi_1 = \varphi_{es} \text{ and } \varphi_2 = \varphi_{ce,2} - \pi & \text{elsewhere} \end{cases}$$

$$= \begin{cases} \frac{\delta_R r_b \pi}{2} (2\theta - \varphi_{e0} - \varphi_{i0} - \pi) & \text{if } \theta \geq \theta^{\text{dis}} \\ \frac{\delta_R r_b \pi}{2} (2\theta + 3\pi - \varphi_{e0} - \varphi_{i0}) & \text{if } \theta \leq \theta^{\text{suc}} \\ \frac{\delta_R r_b}{2} (\theta - \varphi_{es}) (\theta - \varphi_{e0} + \varphi_{es} - \varphi_{i0}) & \text{elsewhere} \end{cases} \quad (37)$$

5.2.2. Leakage between the two compression chambers

Radial leakages between the two compression chambers are computed in the case that $\varphi_{ce,3}$ exists (Fig. 15(d)). Then, it follows,

$$S_{R,\text{com-com}} = \delta_R \int_{\varphi_{ce,k}-\pi}^{\varphi_{ce,k}} \rho(\varphi) d\varphi \text{ if } k = \begin{cases} 3 & \text{if } \exists \varphi_{ce,3} \\ 2 & \text{elsewhere} \end{cases} \quad (38)$$

$$= \begin{cases} \frac{\delta_R r_b \pi}{2} (2\theta - \varphi_{e0} - \varphi_{i0} + 5\pi) & \text{if } \theta \leq \theta^{\text{suc}} \\ \frac{\delta_R r_b \pi}{2} (2\theta - \varphi_{e0} - \varphi_{i0} + \pi) & \text{elsewhere} \end{cases}$$

5.2.3. Leakage between the compression and the suction chambers

Radial leakages between the two compression and suction chambers are computed in the case that $\varphi_{ce,3}$ exists (Fig. 15(a)). Then, it follows,

$$S_{R,\text{com-suc}} = h \delta_R \int_{\varphi_{ce,k}}^{\varphi_{\text{max}} - \pi} \rho(\varphi) d\varphi \text{ with } k = \begin{cases} 3 & \text{if } (\exists \varphi_{ce,3}) \\ 2 & \text{elsewhere} \end{cases} \quad (39)$$

$$= \begin{cases} \frac{\delta_R r_b}{2} (\varphi_{\text{max}} - 4\pi - \theta) (\theta + 2\pi + \varphi_{\text{max}} - \varphi_{e0} - \varphi_{i0}) & \text{if } \theta \leq \theta^{\text{suc}} \\ \frac{\delta_R r_b}{2} (\varphi_{\text{max}} - 2\pi - \theta) (\theta + \varphi_{\text{max}} - \varphi_{e0} - \varphi_{i0}) & \text{elsewhere} \end{cases}$$

5.2.4. Leakage between the compression chamber and the outside

Radial leakages between the two compression and outside the compressor are computed if the compression chambers are in contact with the outside and with the suction chamber (Fig. 15(a)) or only with the suction chamber (no leakages anymore with the outside as seen, for example on Fig. 15(b)).

$$S_{R,com-amb} = \begin{cases} h\delta_R \int_{\varphi_{max}-\pi}^{\varphi_{ci,k}} \rho(\varphi) d\varphi & \text{with } k \begin{cases} 3 & \text{if } (\exists \varphi_{ce,3}) \wedge (\varphi_{max} - \pi \leq \varphi_{ci,3}) \\ 2 & \text{if } (\varphi_{max} - \pi \leq \varphi_{ci,2}) \end{cases} \\ 0 & \text{elsewhere} \end{cases} \quad (40)$$

$$= \begin{cases} \frac{\partial R_{fb}}{2} (\theta + 5\pi - \varphi_{max}) \cdot (\theta + 3\pi + \varphi_{max} - \varphi_{e0} - \varphi_{i0}) & \text{if } (\theta \leq \theta^{suc}) \wedge (\varphi_{max} - 5\pi \leq \theta) \\ \frac{\partial R_{fb}}{2} (\theta + 3\pi - \varphi_{max}) \cdot (\theta + \pi + \varphi_{max} - \varphi_{e0} - \varphi_{i0}) & \text{if } \varphi_{max} - 3\pi \leq \theta \\ 0 & \text{elsewhere} \end{cases}$$

5.2.5. *Leakage between the suction chamber and the outside*
Radial leakages between the suction chamber and outside the compressor are computed with the same conditions as the leakages between the compression chamber and the outside of the compressor. It follows,

$$S_{R,suc-amb} = \begin{cases} h\delta_R \int_{\varphi_x}^{\varphi_{max}} \rho(\varphi) d\varphi & \text{with } \varphi_x = \begin{cases} \varphi_{ci,3} & \text{if } (\exists \varphi_{ce,3}) \wedge (\varphi_{max} - \pi \leq \varphi_{ci,3}) \\ \varphi_{ci,2} & \text{if } (\varphi_{max} - \pi \leq \varphi_{ci,2}) \\ \varphi_{max} - \pi & \text{elsewhere} \end{cases} \\ \frac{\partial R_{fb}}{2} (\varphi_{max} - \theta - 4\pi) \cdot (\theta + 4\pi + \varphi_{max} - \varphi_{e0} - \varphi_{i0}) & \text{if } (\theta \leq \theta^{suc}) \wedge (\varphi_{max} - 5\pi \leq \theta) \\ \frac{\partial R_{fb}}{2} (\varphi_{max} - \theta - 2\pi) \cdot (\theta + 2\pi + \varphi_{max} - \varphi_{e0} - \varphi_{i0}) & \text{if } \varphi_{max} - 3\pi \leq \theta \\ \frac{\partial R_{fb}}{2} (2\varphi_{max} - \pi - \varphi_{e0} - \varphi_{i0}) & \text{elsewhere} \end{cases} \quad (41)$$

5.3. Discharge port

Most authors consider the discharge process as symmetrical in order to simplify the computation of the model: the position of the discharge port is located at the central part of scrolls. This assumption is very strong and can make the theoretical results wrong with regard to the experiment: for a real discharge process, the position of the discharge port makes the pressures in the compression chambers different.

The discharge flow process has been studied and explained in *Nieter and Gagne (1992)*, but the authors do not give the mathematical expression of the discharge area: only a qualitative description is given. This paper proposes an approach to take into account the discharge flow dynamics.

For the investigated compressor, the discharge port matches the interpolating circle introduced in Section 2.2. The representation of the discharge port is consequently given by (7).

During the discharge process, several cases can be distinguished:

- (1) the discharge port is located only in the discharge chambers as shown in Fig. 16(a). There are no leakages between the compression chamber and the discharge port (i.e., $S_{dis,3} = 0$);
- (2) the discharge port is divided between the compression and discharge chambers. In this case three kinds of leakages exist as shown in Fig. 16(b).

As a first approximation, the following assumptions are given:

H 1 The thickness of the end of the scroll is negligible compared to the diameter of the discharge port.

H 2 When the overall discharge chamber area $2A_{dis}$ (i.e., $2V_{dis}/h$) is greater than the discharge port area, all the leakage through the discharge port comes from the discharge chambers.

$$H1 \Rightarrow S_{dis,1}(\theta) + S_{dis,2}(\theta) + S_{dis,3}(\theta) = \pi r_c^2 \quad (42)$$

$$S_{dis,3}(\theta) = \begin{cases} 0 & \text{if } A_{dis}(\theta) \geq \pi r_c^2 \\ \pi r_c^2 - V_{dis}(\theta)/h & \text{elsewhere} \end{cases} \quad (43)$$

$$S_{dis,2}(\theta) \approx \begin{cases} \text{asin}\left(\frac{l_{dis}(\theta)}{2r_c}\right) r_c^2 - \frac{1}{2} l_{dis}(\theta) \sqrt{r_c^2 - \left(\frac{1}{2} l_{dis}(\theta)\right)^2} & \text{if } A_{dis}(\theta) \geq \pi r_c^2 \\ \frac{1}{2} V_{dis}(\theta)/h & \text{elsewhere} \end{cases} \quad (44)$$

$$S_{dis,1}(\theta) = \begin{cases} \pi r_c^2 - S_{dis,2}(\theta) & \text{if } A_{dis}(\theta) \geq \pi r_c^2 \\ \frac{1}{2} V_{dis}(\theta)/h & \text{elsewhere} \end{cases} \quad (45)$$

where $A_{dis}(\theta) = V_{dis}(\theta)/h$ is given by (30).

6. Thermodynamic model

Once the geometry is known, the physical behaviour of each component given in Fig. 8 page 1 has to be modelled. As shown in Fig. 8, two kinds of components exist: control volume components with their volume variation given as a function of the orbiting angle and leakage components where the leakage area is given as a function of the orbiting angle.

6.1. Model of the control volume component

The model of a control volume is based on energy and mass conservation. If the kinetic energy is neglected, the internal energy in the control volume can be written,

$$E = M c_v T \quad (46)$$

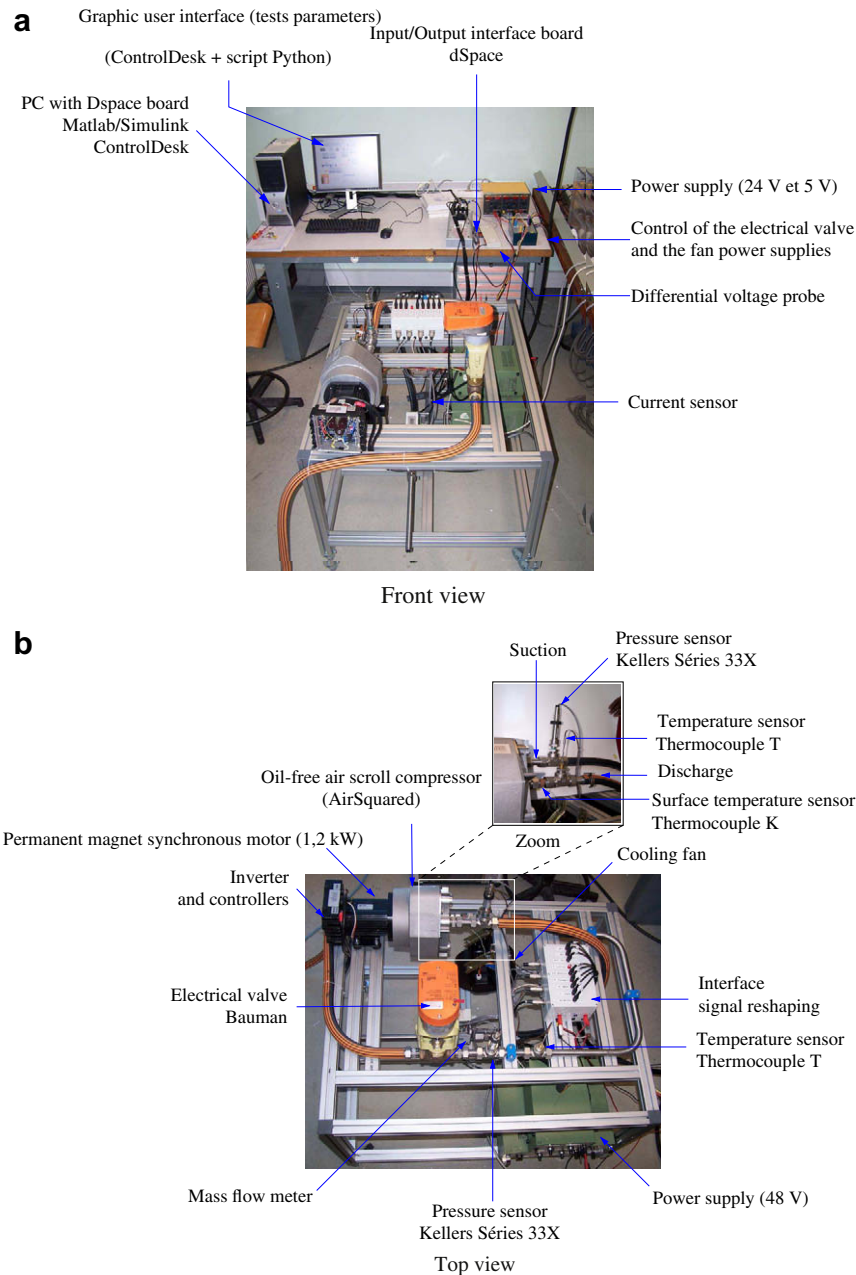


Fig. 17 – Photograph of the scroll compressor test bench (UTBM, France).

where M is the mass of the gas, c_v its specific heat at constant volume and T , the temperature of the gas.

The internal energy is changed due to (Gravensen et al., 1998):

- (1) the work done by changes in the volumes: $-p \dot{V}$,
- (2) the energy transported into and out of the chamber through its leakage areas. If it is assumed that the flow through the leakages is adiabatic, the energy inside the flow is qH where q is the mass flow and H its enthalpy which can be written also $H = c_p T$ where c_p is the specific heat of the gas at constant pressure,
- (3) dissipation and energy losses to the external environment, \dot{Q} .

Then, the energy variation inside a control volume can be written,

$$\dot{E} = -p\dot{V} + \sum_i c_p q_i T_i + \dot{Q} \quad (47)$$

It has to be noticed that the mass flows can be either positive or negative depending on the pressure inside and outside the chamber. If the pressure in the chamber is greater than the pressure outside, the gas will flow out of the chambers ($q < 0$): its temperature will be the chamber temperature T . In the other case, if the outside pressure is greater than the chamber pressure, the gas will flow into the chamber ($q > 0$): its temperature will be the outside temperature (adjacent chamber or atmospheric conditions).

If \dot{Q} is neglected, (46) and (47) can be combined together giving an ordinary differential equation relating control volume pressure p and temperature T :

$$V \frac{dp}{dt} = \gamma r \sum_i q_i T_i - \gamma p \frac{dV}{dt} \quad (48)$$

where r stands for the gas constant ($c_p - c_v$) and γ for the gas specific heat ratio.

The time derivative of the volume can be written as a function of the rotational speed Ω of the compressor and angular derivative of the volume which is calculated analytically, that is,

$$\frac{dV}{dt} = \frac{dV}{d\theta} \cdot \frac{d\theta}{dt} = \frac{dV}{d\theta} \cdot \Omega \quad (49)$$

Considering (49), (48) becomes,

$$V \frac{dp}{dt} = \gamma r \sum_i q_i T_i - \gamma p \frac{dV}{d\theta} \cdot \Omega. \quad (50)$$

$$q = \begin{cases} C_d A p_{up} \sqrt{\frac{2\gamma}{(\gamma-1)RT_{up}} \left(\frac{p_{down}}{p_{up}} \right)^{\frac{2}{\gamma}} - \left(\frac{p_{down}}{p_{up}} \right)^{\frac{\gamma+1}{\gamma}}} & \text{if } \frac{p_{down}}{p_{up}} \geq \left(\frac{2}{\gamma+1} \right)^{\frac{\gamma}{\gamma-1}} \\ C_d A p_{up} \sqrt{\frac{\gamma}{RT_{up}} \left(\frac{2}{\gamma-1} \right)^{\frac{\gamma+1}{\gamma-1}}} & \text{elsewhere} \end{cases} \quad (53)$$

Finally, the mass conservation equation can be written:

$$\frac{dM}{dt} = \frac{d\rho V}{dt} = \frac{d}{dt} \left(\frac{pV}{rT} \right) = \sum_i q_i \quad (51)$$

Rearranging (51), a second equation relating the pressure and the temperature of the chamber can be given,

$$\frac{dT}{dt} = \frac{T}{p} \frac{dp}{dt} + \frac{T}{V} \frac{dV}{d\theta} \Omega - \frac{rT^2}{pV} \sum_i q_i \quad (52)$$

From (50) and (52) pressure and temperature can be computed in each chamber knowing all the mass flows through its leakages areas.

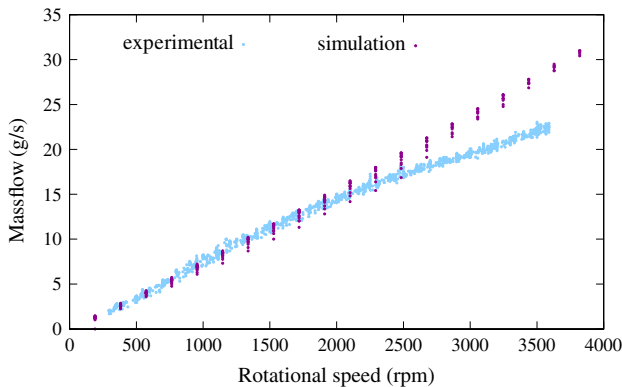


Fig. 18 – Comparison between experimental and simulated mass flows for all operating points (pressures).

The control volume components impose the pressure and temperature at their boundaries; whereas, the leakage components impose the mass flows.

The gas model is for gases which behave ideally at specified operating parameters. Consequently, this gas model is not suitable for CO₂ refrigeration systems because CO₂ behaves mostly non-ideally because they operate at high pressure and transcritical process. However, for the investigated air compressor which works at low pressures and flow rate, this model is suitable.

6.2. Model of the leakage component

The nozzle flow equation (isentropic assumption) is used to calculate the leakages between the chambers. It has to be noticed that suction and discharge processes are considered as leakages in the model.

The mass flow through a leakage area is (Yanagisawa et al., 1990),

where C_d is the flow coefficient and A the leakage area. p_{up} and p_{down} stand for the maximum and minimum pressures, respectively, across the leakage component.

The leakage component imposes the mass flow whereas the chamber imposes the pressure across the leakage component.

7. Simulation and experimental comparison

7.1. Simulation language

The compressor model has been implemented in a simulation software which supports the VHDL-AMS² simulation language.

The IEEE 1076.1 language, informally known as VHDL-AMS, is a superset of IEEE Std 1076-1993 (VHDL) that provides capabilities for describing and simulating continuous time and mixed-signal systems with conservative and nonconservative semantics for the continuous time portion of the system. The language supports many abstraction levels in electrical and nonelectrical energy domains. The modelled continuous time systems are lumped systems that can be described by ordinary differential equations and algebraic equations (DAEs). The language does not specify any particular technique to solve the equations, but it rather defines the results that must be achieved. The solution of the equations

² IEEE standard Very High Speed Integrated Circuit Hardware Description Language – Analog and Mixed Signal Extensions.

may include discontinuities. Interaction between the discrete time part of a model and its continuous time part is supported in a flexible and efficient manner. The authors (Blunier and Miraoui) present a VHDL-AMS model in the reference [Blunier and Miraoui \(2007\)](#).

The VHDL-AMS is designed to fill a number of needs in the process design ([Ashenden et al., 2003](#)):

- (1) it allows description of the structure of a system, that is, how it is decomposed into subsystems from different disciplines and how those subsystems are interconnected,
- (2) it allows the specification of the function of a system using familiar programming language and equation forms,
- (3) it allows the design of a system to be simulated before being manufactured: designers can compare alternatives and test for correctness without the delay and expense of hardware prototyping,
- (4) it allows the detailed structure of a design to be synthesized from a more abstract specification, allowing designers to concentrate on more strategic design decisions and reducing time to market.

Moreover, the language is suited to express plant models and control algorithms needed for car manufacturers and suppliers. In other words, it is able to communicate the manufacturer's requests and suppliers' solutions and it is suitable for model exchange within companies or between researchers and companies.

Several commercial simulators are available today like SystemVision (Mentor Graphics), Smash (Dolphin Integration), Simplorer (Ansoft) and SaberHDL (Synopsis).

For this model the SMASH solver and simulator (v.5.9) from Dolphin Integration has been used because it offers the best support for the VHDL-AMS standard.

7.2. Simulation process

The model topology has already been given in [Fig. 8](#) (page 1). Each chamber or leakage component has its own geometrical law but the physical behaviours are the same.

To simulate the system, end conditions and initial conditions have to be given. In this case, atmospheric pressure and temperature are both the end and the initial conditions. As explained above in sec 3, the compression process is periodic for each chamber: it starts at $\theta = \theta^{\text{suc}}$ and ends at $\theta = \theta^{\text{suc}} + 2\pi$. After one complete cycle, the n th chamber becomes the $(n+1)$ th chamber: the suction chamber becomes the compression chamber, the compression chamber becomes the discharge chamber. After each cycle (i.e., when $\theta = \theta^{\text{suc}}$), the final conditions (pressure and temperature) of the chamber n are transferred to the chamber $n+1$. The suction chamber is reinitialized at the atmospheric pressure and temperature.

As shown in [Fig. 8](#), the outlet pressure is imposed by the pipe (considered as a control volume with a constant volume). The outlet mass flow is imposed by the valve (considered as an isentropic nozzle) where the section area can be controlled. It is then possible to control the pressure inside the pipe by means of the valve and the mass flow by means of the rotational speed: in this case, all operating points of the compressor can be reached.

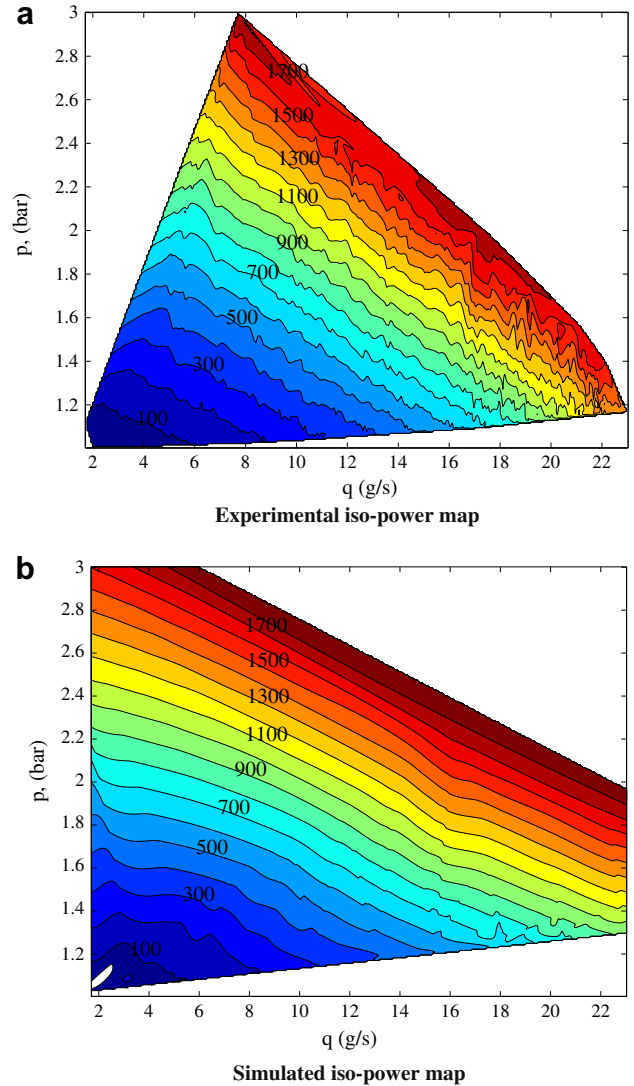


Fig. 19 – Experimental and simulated compressor iso-power maps.

The mechanical compressor power P is computed as follows ([Yanagisawa et al., 1990](#)):

$$P = \sum_{i \in \{\text{suc, com, dis}\}} -(p_i - p_{\text{suc}}) \frac{dV}{d\theta} \Omega \quad (54)$$

The mechanical torque Γ can be deduced from the power using the following formula,

$$\Gamma = \frac{P}{\Omega} \quad (55)$$

7.3. Comparison between simulation and experiment

[Fig. 17](#) shows the photo of an air compressor test bench for the fuel cell applications at the UTBM³. This compressor is to be used for fuel cell air supply, it has been characterized and its results have been compared with simulations.

³ Université of Technologie de Belfort-Montbéliard, France.

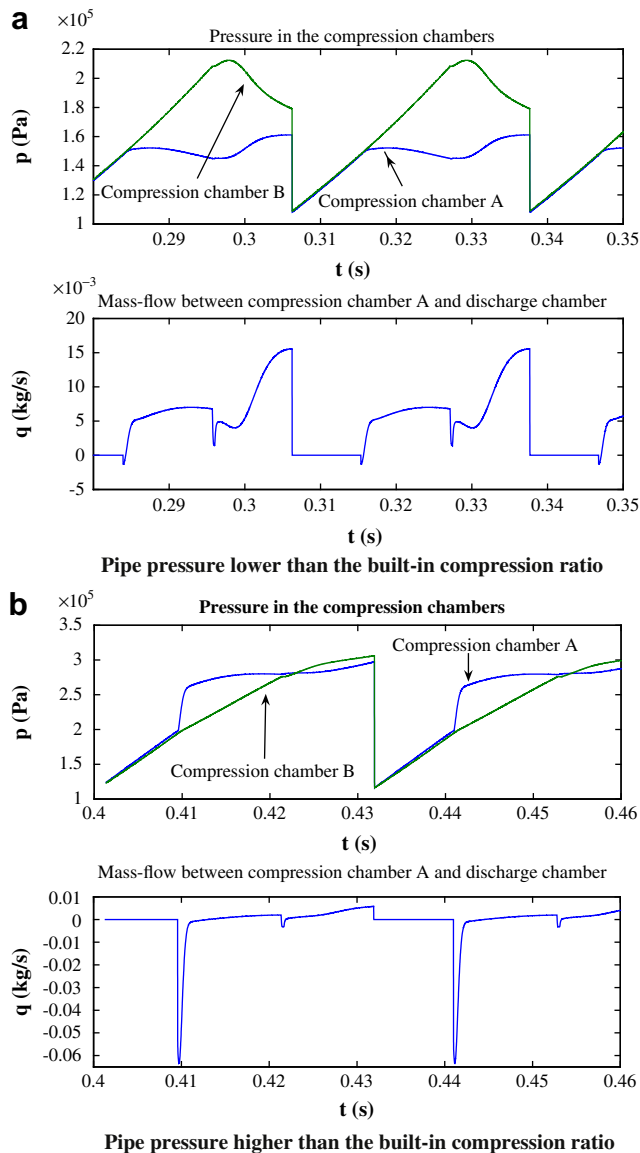


Fig. 20 – Pressures inside the compression chambers.

As for the simulation, the rotational speed of the compressor and the opening of the outlet valve can be controlled accurately. The test bench has been automated with a Dspace system using Matlab/Simulink and a Python script. The test have been run for several compressor speeds and valve positions, recording for each operating point in steady state, the average pipe pressure and temperature, the mass flow rate and the compressor power.

Fig. 18 shows the comparison between the experimental and the simulated mass flows as a function of the rotational speed for all operating points (pressures). It can be seen that the predicted mass flow is very good up to 2500 rpm. The differences can be explained by the internal leakage areas estimations which were assumed to be constant: it does not seem that this is the case as mentioned in (8). This will be included for the next step in a more refined model.

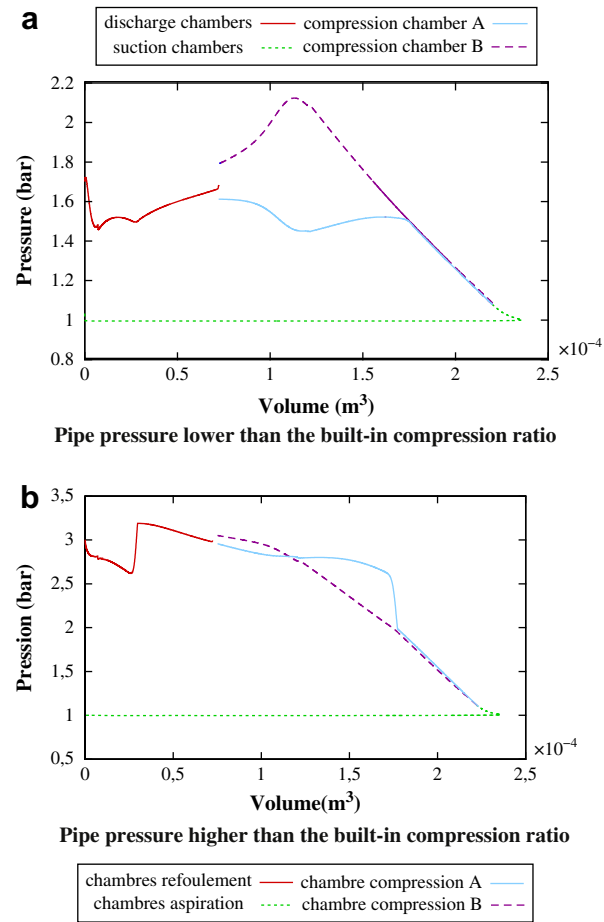


Fig. 21 – PV-diagrams of the compressor.

The experimental and simulated iso-power maps are given on Fig. 19(a) and Fig. 19(b), respectively. The model fits well with experimental data: some differences still remain. These differences come on the one hand from the leakage estimation as explained above, but also, on the other hand, because the thermal interaction with the surrounding parts have been neglected. This can also be included for the next step in a more refined model.

As explained above, the model does not consider the compression process as symmetrical: one of the compression chambers (compression chamber A as seen on Fig. 8) starts to open in the pipe before the other one. In the simulation, two cases have been tested:

- the first (Fig. 20(a)) is when the pipe pressure is lower than the compression chamber pressure: as seen on the figure, when the compression chamber A starts to open into the pipe, the air flows from the compression chamber to the pipe, resulting in a pressure drop inside the compression chamber. The corresponding P–V diagram is given in Fig. 21(a).
- the second (Fig. 20(b)) is when the pipe pressure is higher than the compression chamber pressure: as seen on the figure, when the compression chamber B starts to open into the pipe, the air flows from the pipe to the compression

chamber, resulting in a pressure increase inside the compression chamber. In this case the air is compressed again with resulting energy losses. The corresponding P–V diagram is given in Fig. 21(b).

The suction process has been analysed for several rotational speeds (Fig. 22). As in Nieter (1988), this model has an important capability of showing the effects of the shaft speed on the suction efficiency: the effects of kinematics and flow dynamics are predicted and show that the suction gas actually starts being compressed before the outer scroll wrap tip seals off the displacement volume of gas at the start of compression. This phenomena is known

as the supercharging effect. The suction process is studied together with compression and discharge chambers which makes a difference with Nieter's model: Nieter deals only with the suction process and does not consider the compression chamber where the pressure is greater than the atmospheric pressure and where leakages can occur. In the results given on Fig. 22, it can be seen that the pressure at the start of suction (phase shifted to $\theta = 0$), is greater than the atmospheric pressure because the gas flows from the compression chamber into the suction chamber: this phenomena has not been reported in Nieter (1988).

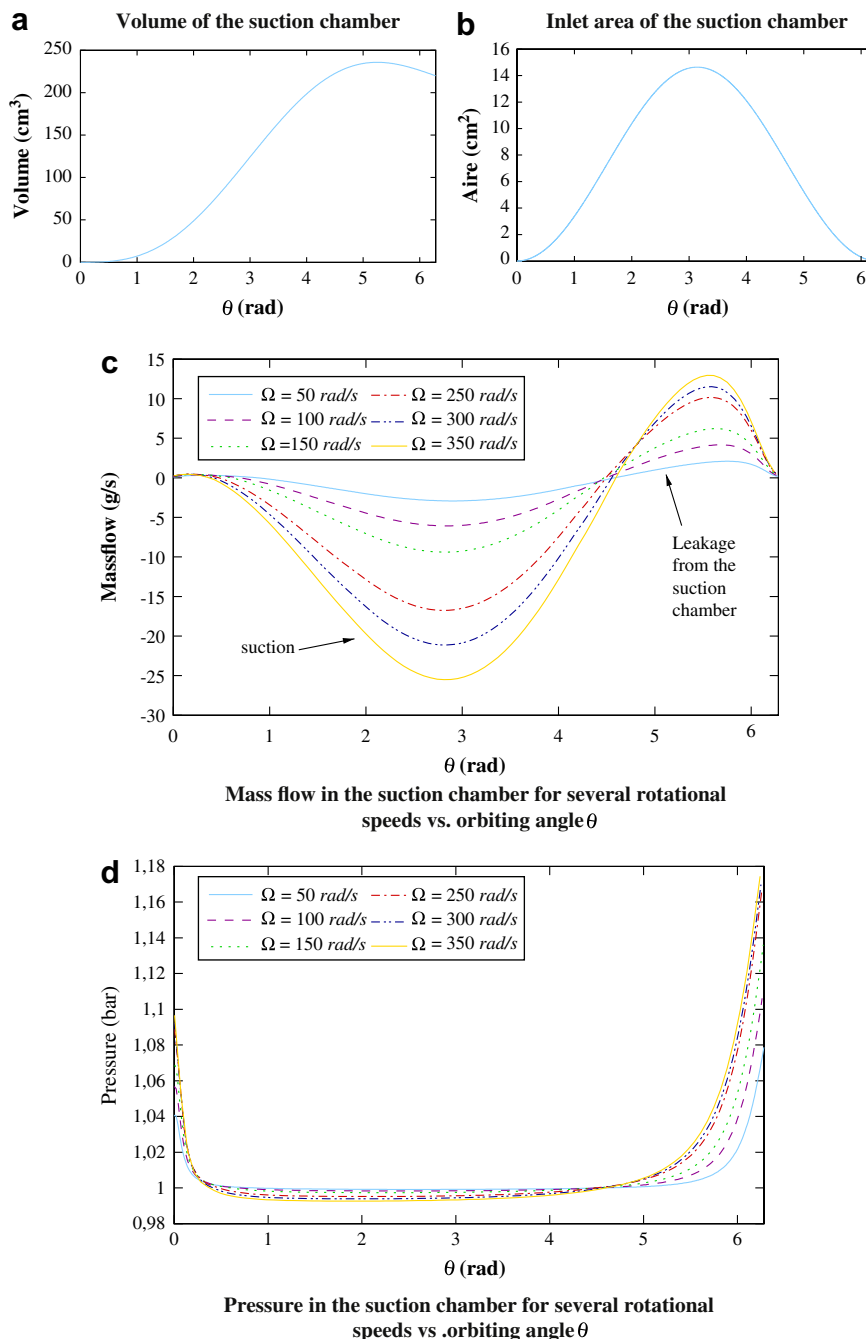


Fig. 22 – Suction process for several rotational speeds.

8. Conclusion

This paper proposes an original way to describe the geometry of the scroll wraps in which the symmetries are easily exploited to establish a thermodynamic model of the scroll compressor. The advantages of the model are the following: (1) the chamber volumes are analytically described without assuming any special case for the initial involute angles, (2) the flank and radial leakages are taken into account, (3) the discharge process is not considered as symmetrical. However, the extended part of the scroll is assumed to be an arc of circle as proposed by most of the authors (Halm, 1997; Yanagisawa et al., 1990; Wang et al., 2005; Blunier et al., 2006).

A complete geometrical description of the scroll is given, together with its validation. A novel reference frame is introduced and the points of conjugacy are expressed. The compression process is described in detail and the estimation of the chamber volumes and the leakages between them are given respectively. The discharge process is also analysed in detail considering a non-symmetrical discharge process. A simple thermodynamic model of the chambers and leakage components are given neglecting the heat transfers with the surrounding parts. Comparison between simulation and experimental results are given with good agreement.

The model shows its capability to predict asymmetries inside the compression and the discharge process but also the supercharging effect during the suction process. The model allows for the investigation of the influence of leakages and compressor geometrical parameters on the compressor performance and can be used to improve the compressor's design. The model also permit to be used very easily with other gases like CO₂ or other refrigerants in many applications. However, to be used with refrigerant gases at high pressure a model for real gas considering two-phase flow in the leakages is highly recommended.

However, the model does not yet take into account the heat exchanges between chambers and with the surrounding parts. Moreover, leakage areas between the chambers are considered as constant and the results show that for speeds higher than 2500 rpm, the model fails to predict an accurate mass flow. Both of the phenomena will be included to have a more refined model and improve the model accuracy.

Acknowledgments

This work has been produced with the SMASH 5.9 solver from Dolphin Integration Company.

The authors would like to express sincere thanks to the peoples who have contributed to this work:

- Dr. B. Blunier and his thesis advisor Pr. A. Miraoui for the overall analytical model of the Scroll compressor,
- Dr. G. Cirrincione for his help on the mathematical geometry description of the spirales,
- Dr. Y. Hervé for his help in debugging some parts of the VHDL-AMS code.

The authors thanks also PSA-Peugeot-Citroën company for their financial support.

REFERENCES

- Ashenden, P.J., Peterson, G.D., Teegarden, D.A., 2003. *The System Designer's Guide to VHDL-AMS, Analog, Mixed-Signal and Mixed-Technology Modeling*. Morgan Kaufmann Publishers.
- Blunier, B., Miraoui, A., 2007. Modelling of fuel cells using multi-domain VHDL-AMS language. *Journal of Power Sources* 177 (2), 434–450.
- Blunier, B., Miraoui, A. PEM fuel cells air management in automotive applications, *ASME Journal of Fuel Cell Science and Technology*, in press.
- Blunier, B., Cirrincione, G., Miraoui, A., 2006. Novel geometrical model of scroll compressor for the analytical description of the chamber volumes. In: *Proceedings of International Compressor Engineering Conference at Purdue*, no. CO74.
- Blunier, B., Pucci, M., Cirrincione, G., Miraoui, A., 2008a. A scroll compressor with a high performance induction motor drive for the air management of a pemfc system for automotive applications. *IEEE Transactions on Industry Applications* 44, 1966–1976.
- Blunier, B., Pucci, M., Cirrincione, G., Cirrincione, M., Miraoui, A., 2008b. A scroll compressor with a high performance sensorless induction motor drive for the air management of a pemfc system for automotive applications. *IEEE Transaction on Vehicular Technology* 57, 3413–3427.
- Bush, J., Beagle, W., 1992. Derivation of general relationship governing the conjugacy of scroll profiles. In: *Proceedings of International Compressor Engineering Conference at Purdue*, pp. 1079–1088.
- Chen, Y., Halm, N.P., Groll, E.A., Braun, J.E., 2002. Mathematical modeling of scroll compressor – part I: compression process modeling. *International Journal of Refrigeration* 25, 731–750.
- Creux, L., 1905. Rotary engine, U.S Patent 801182.
- Gravensen, J., Henriksen, C., 2001. The geometry of the scroll compressor. *Society for Industrial and Applied Mathematics* 43, 113–126.
- Gravensen, J., Henriksen, C., Howell, P., 1998. Danfoss: Scroll Optimization, Final report. Department of Mathematics, Technical University of Denmark, Lyngby. 32nd European Study Group with Industry.
- Halm, N.P., 1997. Mathematical modeling of scroll compressor, Master's thesis, Herrick Lab., School of Mechanical Engineering, Purdue University.
- Haykin, S., 1998. *Neural Networks: A Comprehensive Foundation*. Prentice Hall PTR, Upper Saddle River, NJ, USA.
- Hirano, T., Hagimoto, K., Maada, M., 1990. Scroll profiles for scroll fluid machines. *MHI Technical Review* 27 (1), 35–41.
- Lee, Y.-R., Wu, W.-F., 1995. On the profile design of a scroll compressor. *International Journal of Refrigeration* 18 (5), 308–317.
- Lee, Y.-R., Wu, W.-F., 1996. A study of planar orbiting mechanism and its applications to scroll fluid machinery. *Mechanism and Machine Theory* 31 (5), 705–716.
- Liu, Z., Du, G., Yu, S., Wang, M., 1992. The graphic method of modified wraps of scroll compressor. In: *Proceeding of the international compressor engineering conference at Purdue*, pp. 1099–1106.
- Morishita, E., Sugihara, M., Inaba, T., Nakamura, T., Works, W., 1984. Scroll compressor analytical model. In: *Purdue International Compressor Engineering Conference Proceedings*, pp. 487–495.
- Nieter, J.J., 1988. Dynamics of scroll suction process. In: *Purdue International Compressor Engineering Conference Proceedings*, pp. 165–174.

- Nieter, J.J., Gagne, D.P., 1992. Analytical modeling of discharge flow dynamics in scroll compressors. In: Purdue International Compressor Engineering Conference Proceedings, pp. 85–95.
- Tojo, K., Ikegawa, M., Maeda, N., Machida, S., Shuubayashi, M., 1986. Computer modeling of scroll compressor with self adjusting back-pressure mechanism. In: Purdue International Compressor Engineering Conference Proceedings, pp. 872–886.
- Wang, B., Li, X., Shi, W., 2005. A general geometrical model of scroll compressors based on discretional initial angles of involute. *International Journal of Refrigeration* 28, 958–966.
- Yanagisawa, T., Cheng, M., Fukuta, M., Shimizu, T., 1990. Optimum operating pressure ratio for scroll compressor. In: Proceeding of the International Compressor engineering conference at Purdue, pp. 425–433.
- Zhenquan, L., Guirong, D., Zhiyong, Q., Jianfeng, G., 1994. The conjugacy analysis of modified part of scroll profiles. In: Proceedings of International Compressor Engineering Conference at Purdue, West Lafayette, Indiana, USA, Vol. 1. R. W.H. Laboratories, pp. 479–484.